Published in final edited form as:
*Inorg Chem*. 2010 April 19; 49(8): 3618–3628. doi:10.1021/ic901891n.

# Oxygen Activation at Mononuclear Nonheme Iron Centers: A Superoxo Perspective

**Anusree Mukherjee**[†], **Matthew A. Cranswick**[†], **Mrinmoy Chakraborti**[¶], **Tapan K. Paine**[†,#], **Kiyoshi Fujisawa**[‖], **Eckard Münck**[¶], and **Lawrence Que Jr.**[†,*]

[†] Department of Chemistry and Center for Metals in Biocatalysis, University of Minnesota, 207 Pleasant St. SE, Minneapolis, MN 55455

[‖] Department of Chemistry, Graduate School of Pure and Applied Sciences, University of Tsukuba, Tsukuba 305-8571, Japan

[¶] Department of Chemistry, Carnegie Mellon University, 4400 Fifth Avenue, Pittsburgh, PA 15213

## Abstract

Dioxygen activation by iron enzymes is responsible for many metabolically important transformations in biology. Often a high-valent iron-oxo oxidant is proposed to form upon dioxygen activation at a mononuclear nonheme iron center, presumably via intervening iron-superoxo and iron-peroxo species. While iron(IV)-oxo intermediates have been trapped and characterized in enzymes and models, less is known of the putative iron(III)-superoxo species. Utilizing a synthetic model for the 2-oxoglutarate-dependent monoiron enzymes, [($Tp^{iPr2}$)$Fe^{II}$($O_2CC(O)CH_3$)], we have obtained indirect evidence for the formation of the putative iron(III)-superoxo species, which can undergo one-electron reduction, hydrogen-atom transfer, or conversion to an iron(IV)-oxo species, depending on the reaction conditions. These results demonstrate the various roles the iron(III)-superoxo species can play in the course of dioxygen activation at a nonheme iron center.

## Introduction

Many nonheme iron enzymes act by catalyzing the activation of dioxygen in many metabolically important functions.[1–5] Such functions include the hydroxylation of methane in methanotrophs, the desaturation of fatty acids in plants, DNA and RNA repair, the biosynthesis of β-lactam antibiotics, and sensing hypoxia in mammalian cells to signal the formation of blood vessels. As a consequence, this subject has attracted the interest of bioinorganic chemists for many years (see, for example, the 2007 special issue on oxygen activation of *Acc. Chem. Res.* Vol. 40, issue 7 edited by Wonwoo Nam). At the simplest level, this process can be construed as a series of electron transfer steps with $O_2$ progressing through superoxo, peroxo, and oxo states concomitant with an increase in the formal iron oxidation state. This notion is illustrated in Scheme 1 for the proposed mechanism for the 2-oxoglutarate (2-OG)-dependent enzymes.[6, 7] The efforts of Bollinger and Krebs have established that oxoiron(IV) intermediates are in fact generated in the catalytic cycles of four 2-OG-dependent enzymes

Corresponding author: larryque@umn.edu.
[#]Current Address: Department of Inorganic Chemistry, Indian Association for the Cultivation of Science, 2A&2B Raja S. C. Mullick Road, Jadavpur, Kolkata-700032, India.

Supporting information available: Crystallographic data for **1** and **2** and a table comparing their parameters, ESI-MS data along with simulations, $^1$H-NMR spectra showing the decarboxylation of the benzoylformate, and Mössbauer spectra of the monomeric high-spin-$Fe^{III}$-species observed in the oxygenation of **1** at −40 °C are available in the SI. These materials are available free of charge via the internet.

and that high-valent iron serves as the oxidant for the key C–H bond cleavage step in many reactions.[8–10]

In contrast, much less is known about the nature of the Fe–$O_2$ adducts that must initially form in the course of dioxygen activation. Often these species are considered merely as pass-through points en route to the high-valent intermediates that have been the focus of current efforts. However recent developments suggest that more attention should be paid to some of these adducts, as they may perform more important roles than earlier construed.[11]

Interestingly, a number of possible functions has been proposed for the bound $O_2$ in the mechanisms of these nonheme iron enzymes.[4] For Rieske dioxygenases like naphthalene 1,2-dioxygenase (NDO), it serves to accept an electron from NADH via a nearby Rieske iron-sulfur cluster to form an iron(III)-peroxo intermediate,[12–14] completely analogous to its role in the cytochrome P450 mechanism. For the large 2-OG-dependent enzyme family, the bound $O_2$ acts as a nucleophilic superoxide and attacks the electrophilic keto carbon of 2-OG.[6] For extradiol cleaving dioxygenases like homoprotocatechuate 2,3-dioxygenase (HPCD), the ligated $O_2$ is proposed to accept an electron from the adjacently bound catecholate substrate using the metal center as conduit to generate an iron(II)/substrate radical/superoxo complex that leads to an alkylperoxoiron(II) intermediate.[15] For isopenicillin N synthase (IPNS)[11] and hydroxyethylphosphonate dioxygenase (HEPD),[16] the bound $O_2$ is proposed to initiate the 4e-oxidation of substrate by abstracting an H-atom from the substrate; similar H-atom abstractions by copper-superoxo species are proposed for dopamine hydroxylase and peptidyl amidating monooxygenase.[17, 18] How an Fe–$O_2$ adduct can be tuned to perform such a variety of functions is a fascinating question for further investigation.

To date spectroscopic evidence is available for only two superoxo intermediates among iron enzymes. One example derives from HPCD, but the superoxo intermediate is that derived from the Mn-substituted enzyme.[19] The Mn substitution affords an equally active enzyme[20] and has the advantage that a Mn(II)–$O_2$ adduct would be expected to be EPR active. Indeed, rapid-freeze-quench samples of the reaction of Mn-HPCD-native substrate complex with $O_2$ obtained 15 ms after mixing gave rise to a short-lived $S = 5/2$ species in ~5% yield.[19] Spectral analysis and comparison with the unreacted Mn-HPCD-substrate complex led to its assignment as a Mn(III)-radical species with the radical favored to be a superoxide. A later intermediate is also observed at higher conversion and proposed to be a Mn(II)-alkylperoxo species that is further along on the reaction pathway. Analogous intermediates presumably form with native Fe-HPCD but will require alternative methods for detection.

The other superoxo intermediate is observed for *myo*-inositol oxygenase (MIOX), the mammalian enzyme that carries out the 4e-oxidation of *myo*-inositol to D-glucoronate by cleaving the C1–C6 bond.[21] X-ray crystallography reveals MIOX to have a carboxylate-bridged diiron active site,[22] which is shown to be in the Fe(II)Fe(III) state by EPR and Mössbauer measurements.[23] In the crystal structure of the enzyme-substrate complex,[22] *myo*-inositol binds as a bidentate ligand to one iron, presumably the iron(III) site to activate the substrate. $O_2$ is then proposed to bind at the other iron, presumably the iron(II) site. Indeed a reversible $O_2$ adduct can be trapped and it exhibits an $S = ½$ EPR signal that is proposed to arise from a diiron(III)-superoxo species.[24] Because the decay of this species can be retarded with the use of deuterated substrate, it is surmised that the superoxo intermediate must be involved in the cleavage of the labeled C–H bond, which likely represents the first step in substrate oxidation.[24] This proposed H-atom abstraction by the iron-bound $O_2$ is in fact analogous to the initial steps postulated in the mechanisms of IPNS and HEPD briefly mentioned above.[11, 16]

X-ray crystallography has been used effectively in some enzymes for visualizing the interaction of $O_2$ with active site iron centers in this family of enzymes.[15, 25, 26] An end-on bound $O_2$ like those seen in heme-$O_2$ adducts.[27] is found in the structure of the 3-hydroxyanthranilate-3,4-dioxygenase (HAD)-inhibitor-$O_2$ complex (Figure 1A),[26] while side-on bound $O_2$ moieties have been observed in crystals of the NDO-indole-$O_2$ and the HPCD-4-nitrocatechol-$O_2$ complexes (Figures 1B and 1C).[15, 25] A consideration of these structures, together with related mechanistic information, suggests to us that the end-on bound $O_2$ in the HAD-inhibitor-$O_2$ complex[26] likely represents an early stage of the Fe-$O_2$ interaction, while the side-on bound $O_2$ adducts correspond to species wherein a subsequent electron transfer step has occurred.

For example, the NDO-indole-$O_2$ adduct (Fig. 1B) is proposed to be an iron(III)-peroxo species that derives from one-electron reduction of the initial Fe–$O_2$ adduct by the nearby reduced Rieske $Fe_2S_2$ cluster. The O–O bond distance is 1.46 Å and the Fe–O distances are 1.7 and 2.0 Å,[25] consistent with an iron(III)-$\eta^2$-peroxo assignment.[28, 29] This difference in Fe–O bond lengths suggests that the more distal oxygen atom may be protonated. The bound $O_2$ is found to be in an ideal geometry to attack the substrate C=C bond to afford the *cis*-dihydrodiol product (Scheme 2). The *cis*-dihydroxylation may occur via a concerted mechanism where the O–O bond cleaves simultaneously with the formation of the two C–O bonds or via a stepwise pathway involving initial O–O bond cleavage and subsequent attack of the C=C bond by the resulting high-valent iron-oxo oxidant.[30]

There is strong crystallographic evidence for a different electron transfer event for the HPCD-4-nitrocatechol-$O_2$ adduct. In this case, the bound $O_2$ has a 1.3 Å O–O distance, the Fe–O distances average 2.5 Å, and the bound 4-nitrocatecholate ion has lost its aromaticity and become nonplanar (Figure 1C and Scheme 2).[15] These observations have been interpreted to indicate electron transfer from the substrate to the bound $O_2$ via the iron(II) center, resulting in a semiquinone-$Fe^{II}$-superoxo complex. The two radical moieties are then postulated to couple forming an alkylperoxoiron(II) intermediate (Figure 1D). Amazingly, the species from this radical-radical coupling step is observed in the two subunits adjacent to the subunit containing the semiquinone-$Fe^{II}$-superoxo structure in the 4-subunit unit cell. An enzyme-product complex is observed in the fourth subunit, demonstrating that HPCD is in fact catalytically active *in crystallo*. These results represent a crystallographic *tour de force* by Kovaleva and Lipscomb[15] and firmly establish the mechanistic notions previously proposed for extradiol cleavage.[31]

The examples listed above demonstrate that much needs to be clarified with respect to the chemistry of Fe–$O_2$ adducts. Biomimetic complexes can be useful in addressing some of these questions, because of their simpler structures and the relative ease of ligand modification. But the big challenge for synthetic bioinorganic chemists is to design model complexes that mimic function and are amenable for mechanistic dissection; only then can they help shed light on the questions raised by the crystallographic results.

To date there is only a handful of well characterized synthetic Fe–$O_2$ adducts with nonheme ligand environments. The three for which crystal structures are available all represent 1,2-peroxo-bridged diiron(III) complexes obtained from the reaction of $O_2$ with iron(II) precursors.[32–34] It is plausible that these adducts form via the initial interaction of $O_2$ with one of the two iron atoms, but no evidence is currently available for such a 1:1 Fe–$O_2$ adduct in the course of forming any of these three complexes.

However, in the case of a related diiron(II) precursor $[Fe^{II}_2(\mu\text{-}OH)_2(6\text{-}Me_3\text{-}TPA)_2]^{2+}$ (Scheme 3), its oxygenation appears to be more controlled to allow transfer of one electron at a time.[35] Indeed a superoxo intermediate can be stabilized at −80 °C, which converts to the well characterized 1,2-peroxo-bridged intermediate $[Fe^{III}_2(\mu\text{-}O)(\mu\text{-}1,2\text{-}O_2)(6\text{-}Me_3\text{-}TPA)_2]^{2+}$ upon

warming to −60 °C.[35] The superoxo intermediate is characterized by a ν(O–O) Raman mode found at 1310 $cm^{-1}$ that downshifts 71 $cm^{-1}$ with $^{18}O_2$. A doublet pattern is observed for the ν(O–O) mode associated with the $^{16}O^{18}O$ isotopomer in the mixed isotope Raman experiment, supporting the notion that the superoxo moiety is bound end-on. The ν(O–O) mode of 1310 $cm^{-1}$ represents the highest frequency yet observed for a metal-bound superoxo species. It is at least 100 $cm^{-1}$ higher than those observed for $O_2$ adducts of heme proteins, synthetic iron porphyrins, and biomimetic copper complexes.[27, 36] The smaller extent of electron transfer from metal to bound $O_2$, as reflected by the higher ν(O-O) frequency, can be easily rationalized by the fact that the iron centers in $[Fe^{II}_2(\mu\text{-}OH)_2(6\text{-}Me_3\text{-}TPA)_2]^{2+}$ are the most Lewis acidic of the metal centers that give rise to superoxo intermediates. Like their copper-superoxo countertparts,[37–40] this intermediate is reactive even at −80 °C and can abstract an H-atom from 2,4-di-*tert*-butylphenol,[35] a reactivity that stands in stark contrast to the inability of the corresponding peroxo intermediate to react with the same phenol at −60 °C.

The observed quantitative conversion of $[Fe^{II}_2(\mu\text{-}OH)_2(6\text{-}Me_3\text{-}TPA)_2]^{2+}$ to $[Fe^{III}_2(\mu\text{-}O)(\mu\text{-}1,2\text{-}O_2)(6\text{-}Me_3\text{-}TPA)_2]^{2+}$ suggests that the intervening superoxo intermediate must result from one-electron transfer from the diiron(II) center to the bound $O_2$ to form an iron(II)iron(III) superoxo adduct. As expected, this species is EPR silent, presumably due to antiferromagnetic coupling. Unfortunately, it has not been possible to ascertain the diiron oxidation state by Mössbauer spectroscopy, because the superoxo intermediate forms only in $CH_2Cl_2$, a solvent that severely hampers the application of this technique. Related chemistry has been reported for diiron(II) complexes of carboxylates that are appended to dendrimers, which provide a hydrophobic environment to surround and protect the diiron center.[41] For these complexes, $O_2$ binding results in the formation of an EPR-silent intermediate that exhibits two Mössbauer doublets corresponding to an antiferromagnetically coupled iron(II)iron(III) center. Unfortunately in this case, no resonance Raman data could be obtained.

One of the synthetic Fe–$O_2$ adducts that have been characterized crystallographically is $[Fe^{III}_2(Tp^{iPr2})_2(O_2CR)_2(O_2)]$,[34] which derives from a mononuclear precursor $[Fe^{II}(Tp^{iPr2})(O_2CR)]$ first reported by Kitajima.[42, 43] By analogy to the established mechanism for forming a (μ-1,2-peroxo)dicopper complex,[44] an iron(III)superoxo species would seem to be a highly plausible intermediate, but no evidence for this complex has been reported. Related to this complex are $Fe^{II}(Tp^{R2})$ complexes (R = Me or Ph) of α-ketocarboxylates that serve as structural and functional models for the 2-OG-dependent enzymes. These complexes have been found to react with $O_2$ and undergo oxidative decarboxylation of the bound α-ketocarboxylate. This reaction produces a presumed high-valent iron-oxo oxidant capable of intramolecular ligand hydroxylation or intermolecular olefin epoxidation or hydrocarbon dehydrogenation.[45–49] Studies of the $Fe(Tp^{Ph2})$ system showed that the rate of reaction increased as a more electron withdrawing substituent was introduced into the α-ketocarboxylates. This behavior was rationalized by Mehn et al. as indicating the rate-limiting attack by a nucleophilic superoxide on the electrophilic keto carbon. In this paper, we describe two complexes, $[Fe^{II}(Tp^{iPr2})(O_2CC(O)R)]$ (**1**, R = $CH_3$; **2**, R = Ph, PRV and BF, respectively), and compare their reactions with $O_2$ with that of the previously characterized $[Fe^{II}(Tp^{iPr2})(O_2CPh)]$ (**3**) to gain insight into what role a superoxoiron(III) intermediate may play in dioxygen activation reactions of nonheme iron complexes.

## Results and Discussion

### Synthesis and characterization of 1 and 2

The two complexes, $[Fe^{II}(Tp^{iPr2})(O_2CC(O)CH_3)]$ (**1**) and [FeII($Tp^{iPr2}$)($O_2$CC(O)Ph)] (**2**), were synthesized by mixing equimolar portions of iron(II) salt with $KTp^{iPr2}$, followed by addition of sodium pyruvate (NaPRV) or sodium benzoylformate (NaBF) (see Scheme 3 for ligand structures). Complex **1** exhibits a distinct red color in solution corresponding to a visible

band with an absorption maximum at 500 nm along with two shoulders at 540 and 458 nm (Figure 2). The corresponding transitions in **2** are red-shifted with a maximum at 610 nm, giving rise to a blue solution (Figure 2). These bands in the visible region are assigned to metal-to-ligand charge transfer (MLCT) transitions of an iron(II)-($\kappa^2$-α-ketocarboxylate) unit by analogy to previous work.[47, 50] The MLCT assignment is consistent with the observed red shift upon replacement of the methyl group with a more electron withdrawing phenyl group on the α-ketocarboxylate.[47]

Diffraction quality crystals could be obtained for both **1** and **2**, and their crystal structures are shown in Figure 3. The structure of **1** shows a six-coordinate iron center with a face-capping tridentate $Tp^{iPr2}$, a bidentate PRV, and a methanol solvate. The structure of **2** exhibits a similar iron coordination environment but features a centrosymmetric dinuclear complex where the methanol solvate in the sixth coordination site of **1** is replaced by the carbonyl oxygen atom of the carboxylate of the BF ligand on the adjacent iron unit in **2**. Complex **2** represents in fact the first example of a complex with a $\kappa^3$-bridging mode of BF. The only other example of a $\kappa^3$-bridging mode for an α-ketoacid is found in the structure of $[Fe^{II}_2(6\text{-}Me_3\text{-}TPA)_2(phenylpyruvate)]^{2+}$.[51] In this latter case, the keto group of the phenylpyruvate has become enolized and the ligand is bound as a dianion, as indicated by a C2–C3 bond length corresponding to a double bond. In contrast, the C2–C3 bond of the BF ligand of **2** has a C–C bond length consistent with a C–C single bond (1.475(3) Å) and the BF binds as the monoanionic keto tautomer.

Selected bond lengths are listed in Table 1 and compared with those from related structures. The $Fe–N_{pyrazole}$ bond lengths of **1** and **2** are typical of $Tp^{R,R'}$ complexes with high-spin iron (II) centers.[43, 47, 52] $^1$H-NMR spectra of **1** and **2** support this conclusion as well (see Experimental Section). Both α-ketoacids bind as monoanions, as indicated by the absence of counterions in **1** and **2**. While the observed $Fe–O_{keto}$ bond lengths are comparable to those found for related $[Fe(Tp^{R,R'})(\alpha\text{-ketocarboxylate})]$ complexes, the $Fe–O_{carboxylato}$ bonds are at least 0.14 Å longer than those found for five-coordinate complexes.

The observed nuclearities of **1** and **2** derive from a difference in solvents used for the preparation of the complexes and their recrystallization, $MeOH/CH_2Cl_2$ for **1** and $CH_2Cl_2$/pentane for **2**. These results are consistent with those reported by Kitajima for $[Fe^{II}(Tp^{iPr2})(O_2CPh)]$ (**3**) where **3** crystallized as the five-coordinate complex in pentane and as the six-coordinate solvate in MeCN.[42,43] Indeed FeTp complexes are often found to crystallize as six-coordinate MeCN or pyrazole adducts.[43,47,52] It would thus appear likely that **2** is mononuclear in MeCN solution. In support, the $\lambda_{max}$ for **2** in toluene is observed at 627 nm, somewhat red-shifted relative to that in MeCN (610 nm), whereas the $\lambda_{max}$ for **1** remains unchanged in both of these solvents. The latter observation suggests that a change in solvent polarity does not affect the position of the MLCT band in **1**. The blue shift observed for **2** in MeCN must have a different rationale and can be understood by considering that **2** retains its dimeric structure in the nonpolar toluene solvent but becomes monomeric in the coordinating MeCN solvent. Thus the displacement of the carboxylate oxygen from the other iron unit of dimeric **2** by a stronger-field MeCN ligand to the iron(II) center would be expected to lower the energy of the iron(II) $d_\pi$ orbitals and increase the energy gap for the iron(II)-to-α-ketocarboxylate MLCT transition.

### Reactions of 1 and 2 with dioxygen at room temperature

Bubbling $O_2$ through the red solution of **1** in MeCN at 25 °C resulted in the onset of immediate spectral changes consisting of the loss of the MLCT band at 500 nm and its replacement by an intense near-UV feature with an absorption maximum at 370 nm ($\varepsilon = 6000\ M^{-1}cm^{-1}$) over the course of 15 min (Figure 2). ESI-MS analysis suggested the formation of an alkoxoiron(III) product, as manifested by peaks at *m/z* = 536 and 688 that were observed along with peaks at

*m/z* = 521 and 673. The peak at *m/z* = 521 together with its isotope distribution pattern can be assigned to the $[Fe^{II}(Tp^{iPr2})]^+$ ion. On the other hand, the peak at *m/z* = 536 has a mass and an isotope distribution pattern that correspond to an ion with the composition of $\{[(Tp^{iPr2})Fe^{III}] + O - H\}^+$(see Figure 4 and Figure S1); that is, one hydrogen atom has been replaced by an oxygen atom, suggesting that the hydroxylation of the $Tp^{iPr2}$ ligand in the course of the reaction to form the oxidation product **4**. The most likely hydroxylation site is at one of the 3-isopropyl methine carbons, as this is the weakest C–H bond present in the ligand and is also in the close vicinity of the iron center. Hydroxylation of an isopropyl group of the $Tp^{iPr2}$ ligand would introduce a tertiary alcohol functionality near the iron center and lead to the formation of a metal-alkoxide bond. We thus assign the *m/z* = 536 peak as $[Fe(Tp^{iPr2*})]^+$ where $Tp^{iPr2*}$ represents the $Tp^{iPr2}$ ligand in which the 3° C–H bond of a 3-isopropyl group on the $Tp^{iPr2}$ ligand has been hydroxylated. The peaks at *m/z* = 673 and 688 correspond respectively to the 3,5-diisopropylpyrazole adducts of the ions with *m/z* = 521 and 536. Analogous attack of a 3-isopropyl C–H bond has previously been demonstrated in the reactions of $[Mn^{II}_2(Tp^{iPr2})_2(OH)_2]$ and $[Co^{I}(Tp^{iPr,Me})]$ with $O_2$, with a crystal structure reported for the alkoxomanganese product complex.[53, 54] The yellow chromophore of **4** thus arises from an alkoxo-to-iron(III) charge transfer transition, as observed for $[Fe^{III}(Py5)(OMe)]^{2+}$ ($\lambda_{max}$, 337 nm; ε, 3600 $M^{-1}cm^{-1}$; Py5 = 2,6-bis(bis(2-pyridyl)methoxymethane)pyridine)[55] and $[Fe^{III}(N4Py)(OMe)]^{2+}$ ($\lambda_{max}$, 360 nm; ε, 4000 $M^{-1}cm^{-1}$; N4Py = *N*,*N*-bis(2-pyridylmethyl)bis (2-pyridyl)methylamine)).[56]

Additional corroboration for the ESI-MS results was obtained from $^1$H-NMR analysis of the organic components of the yellow solutions derived from the oxygenation of **1** and **2**, extracted after treatment of the yellow solutions with strong acid. In the case of **2**, quantitative conversion of benzoylformate to benzoate was indicated by the disappearance of peaks characteristic of the *ortho* protons of the benzoylformate at 8.36 ppm and the appearance of corresponding benzoate features at 8.14 ppm (Figure S3). More importantly for both **1** and **2**, NMR features were observed for two pyrazoles, namely 3,5-diisopropylpyrazole (5.90 ppm for the pyrazole-4-H) and 3-isopropenyl-5-isopropylpyrazole (5.84 ppm for the pyrazole-4-H and 5.3 ppm for one of the vinyl C–H protons). These features were found to be in a ratio of 2:1 (Figure 4), showing that one of the three pyrazoles in the $Tp^{iPr2}$ ligand had been modified. Both 3,5-diisopropylpyrazole and 3-isopropenyl-5-isopropylpyrazole were formed upon acid decomposition of the $Tp^{iPr2*}$ ligand. The 3-isopropenyl-5-isopropylprazole most likely derived from dehydration of hydroxylated 3,5-diisopropylpyrazole, as tertiary alcohols are well known to lose water easily upon reaction with acid to generate alkenes. Notably, ESI-MS analysis of the yellow product solution prior to acid decomposition (Figure 4) did not show a prominent peak at m/z = 519 corresponding to the $\{(Tp^{iPr2})Fe^{II} - 2H\}^+$ ion, indicating that 3-isopropenyl-5-isopropylpyrazole was not formed during the initial oxygenation. These NMR results demonstrate the quantitative oxidative decarboxylation of the bound α-keto acid and concomitant formation of an oxidant that carries out the ligand oxidation, as precedented in the oxygenation of $[Fe^{II}(Tp^{Ph2})$(α-ketocarboxylate)] complexes.[46, 47, 51] In the present study, ligand hydroxylation appears to be quantitative.

To further characterize the oxidant responsible for ligand hydroxylation, experiments were carried out in the presence of potential substrates in an attempt to intercept this oxidant intermolecularly. Such interceptions by either dialkyl sulfides or hydrocarbons have been documented in the oxygenation of $[Fe^{II}(Tp^{Ph2})(BF)]$.[49] When the oxygenation of **1** or **2** was performed in the presence of 100 mM tetrahydrothiophene (THT), the intense yellow chromophore associated with $[Fe(Tp^{iPr2*})]^+$ did not form. ESI-MS analysis of this solution revealed only one major peak at *m/z* = 625, whose mass and isotope distribution pattern matched those for $[Fe^{II}(Tp^{iPr2})\{(OS(CH_2)_4\}]^+$ (Figure S2). Tetramethylenesulfoxide was confirmed to be the oxidation product by GC and GC-MS analysis (80% yield with naphthalene as an internal standard). Interestingly, neither thioanisole nor diphenyl sulfide was capable of intercepting

the oxidant, in contrast to what was reported in the oxygenation of [Fe($Tp^{Ph2}$)(BF)];[49] instead the 370-nm chromophore obtained in the absence of any substrate was observed. Thus **1** and **2** are only able to carry out oxo-transfer to THT. Both steric and electronic factors can be used to rationalize the lack of reactivity towards thioanisole and diphenyl sulfide. Clearly the rates of oxo-transfer to these potential substrates are smaller than the rate of intramolecular C–H bond cleavage by the incipient oxidant.

## Reactions of 1 and 2 with dioxygen at −40°C

The reactivities of **1** and **2** with $O_2$ diverge at −40 °C. While the reactivity of **2** with $O_2$ at −40 °C mirrored that at 25 °C, i.e. intramolecular ligand hydroxylation and intermolecular sulfoxidation, this behavior did not apply to **1**. Oxygenation of **1** at −40 °C in MeCN afforded a distinct chromophore with $\lambda_{max}$ at 680 nm ($\varepsilon \sim 1600\ M^{-1}cm^{-1}$/Fe) that was stable for days at this temperature (Figure 5). This green chromophore was very similar to those observed in the oxygenation of [$Fe^{II}(Tp^{iPr2})(O_2CPh)$] (**3**) ($\lambda_{max}$ 682 nm; $\varepsilon = 1700\ M^{-1}cm^{-1}$/Fe) and [$Fe^{II}(Tp^{iPr2})(O_2CCH_2Ph)$] ($\lambda_{max}$ 694 nm; $\varepsilon = 1300\ M^{-1}cm^{-1}$/Fe) in toluene, which was shown by spectroscopy and crystallography to be [$Fe_2(O_2)(Tp^{iPr2})_2(O_2CR)_2$], a complex with a (μ-1,2-peroxo)diiron(III) core supported by two carboxylate bridges.[34, 43]

The resonance Raman (rR) spectrum of the green chromophore from the oxygenation of **1** at −40 °C was thus obtained to determine its similarity to the $O_2$ adduct described by Kitajima.[43] Excitation at 647.1 nm elicited two resonance enhanced vibrations at 889 and 424 $cm^{-1}$ (Figure 6); these were respectively assigned to ν(O–O) and ν(Fe–O) modes of the (μ-1,2-peroxo)diiron(III) unit by their frequencies and $^{18}O$ isotopic shifts, which closely matched those reported for the Kitajima $O_2$ adducts (Table 2). The isotopic shifts observed for these vibrations, from 889 $cm^{-1}$ to 842 $cm^{-1}$ and 424 $cm^{-1}$ to 408 $cm^{-1}$, are in accord with the isotopic shifts predicted for a diatomic oscillator (838 and 405 $cm^{-1}$, respectively), supporting the assignment of the visible absorption band as a peroxo-to-$Fe^{III}$ charge transfer transition (Figure 5). While there are many examples of (μ-$\eta^1$:$\eta^1$-peroxo)diiron(III) complexes in the literature,[2, 57, 58] only a handful derive from dioxygen binding to a mononuclear iron complex.

In order to further corroborate the nature of the $O_2$ adduct, the frozen MeCN solution of the green chromophore was studied with Mössbauer spectroscopy. The zero field spectrum of Figure 7A exhibits two doublets. One doublet ($\Delta E_Q = 3.42(4)$ mm/s, $\delta = 1.21(2)$ mm/s, 40% of Fe) is attributable to a high-spin iron(II) complex and very likely represents the starting material **1**. The second doublet (45% of Fe), outlined by the solid line, has parameters ($\Delta E_Q$ = 1.32(3) mm/s and $\delta = 0.65(2)$ mm/s) very similar to those of the $O_2$ adduct of [$Fe^{II}(Tp^{iPr2})(O_2CCH_2Ph)$] characterized by Kim and Lippard.[34] Studies in strong applied magnetic fields (Figure S4) revealed that the sample contained also a mononuclear $S = 5/2$ $Fe^{III}$ species (10%). The spectra of Figure 7B and C, representing the green chromophore, were obtained by subtracting from the raw data the contributions of the $Fe^{II}$ and $S = 5/2$ $Fe^{III}$ species (see Supporting Information). The solid line in Figure 7B is a spectral simulation based on the assumption that the peroxo intermediate has a diamagnetic ground state. The magnetic splitting at 100 K (Figure 7C) is smaller than at 4.2 K, a feature observed for antiferromagnetically coupled dinuclear $Fe^{III}$ peroxo complexes with *J*-values around 70 $cm^{-1}$ (in the $\mathcal{H} = J\,\mathbf{S_1}\cdot\mathbf{S}_2$ convention; $S_1 = S_2 = 5/2$). The observed diamagnetism in conjunction with the observed exchange interactions demonstrates that the green chromophore is a diiron(III) complex. Our spectral simulation, performed with the 2Spin option of WMOSS, yielded $J = 70 \pm 10\ cm^{-1}$; details of the Mössbauer method for determining J can be found in several papers.[59–61] This *J* value is in good agreement with the value of 66 $cm^{-1}$ determined from variable temperature magnetic susceptibility measurements on the $O_2$ adduct of [$Fe^{II}(Tp^{iPr2})(O_2CPh)$].43 Our studies thus formulate the green chromophore as having an antiferromagnetically coupled high-

spin (μ-1,2-peroxo)diiron(III) unit, as found for other $O_2$ adducts of [$Fe^{II}(Tp^{iPr2})(O_2CR)$] (Table 2).

The formation of the peroxo intermediate from **1** at −40 °C was not affected by the presence of 100 mM THT either before or after oxygenation. This suggests that neither the peroxo intermediate itself nor any of its possible precursors is capable of oxidizing THT. This lack of reactivity is very similar to that observed by Lippard and co-workers in their studies of (μ-1,2-peroxo)diiron(III) intermediates.[63, 64]

However the formation of the peroxo intermediate was prevented by the presence of 2,4,6-tri-*tert*-butylphenol (TBP-H). When the oxygenation of **1** (1 mM) was performed in the presence of even only one equivalent of TBP-H, the green chromophore associated with the peroxo intermediate did not form at all. Instead, sharp peaks characteristic of TBP• were observed at 373 and 400 nm along with a weak broad band at 620 nm, (Figure 8) with intensities corresponding to an 80% yield of the phenoxyl radical. Under these conditions, phenoxyl radical formation occurred within 3 min, with an estimated first order rate constant of 2.1(4) $\times 10^{-2}$ $s^{-1}$. This value did not change significantly with the use of more equivalents of TBP-H, suggesting that the phenoxyl radical formation occurs after the rate determining step that generates the oxidant.

Control experiments showed that the pre-formed (μ-peroxo)diiron(III) species (1 mM in Fe) also decayed in the presence of TBP-H at −40 °C but with complex kinetic behavior. Furthermore the time scale for decay was nearly two orders of magnitude longer (~70-fold). This much slower reaction cannot rationalize the effect of TBP-H in completely preventing peroxo intermediate formation. Instead, TBP-H must react more rapidly with a precursor of the peroxo intermediate to prevent its accumulation. We propose that this more reactive intermediate is the initial $O_2$ adduct of **1**, the formation of which represents the rate-determining step. Following heme precedents, the **1**•$O_2$ adduct can be formulated as an iron(III)-superoxo species, which can abstract a hydrogen atom from phenol. Such H-atom abstractions have been observed for other metal-superoxo species. [35,39]

Interestingly, the oxygenation of [$Fe^{II}(Tp^{iPr2})(O_2CPh)$] in the presence of as much as 100-fold excess of TBP-H did not prevent formation of the corresponding peroxo intermediate, which suggests that TBP-H is unable to intercept the corresponding iron(III)-superoxo species in this case before it reacts with residual iron(II) precursor. However there are some differences in the conditions under which the respective peroxo intermediates of **1** and **3** can be observed. In the latter case, formation of the peroxo intermediate was observed upon oxygenation of the iron(II) precursor in toluene but not in MeCN.[43] Kitajima conjectured that the likely coordination of MeCN to the metal may inhibit $O_2$ binding to the coordinately saturated iron (II) center. Clearly the solvent MeCN does not play such an inhibitory role in the case of **1**, as a good yield of the peroxo intermediate was observed in MeCN. In fact, only a 10% yield of the peroxo intermediate was obtained for the oxygenation of **1** at −40 °C in toluene. The fact that TBP-H fails to inhibit peroxo intermediate formation in the case of **3** suggests that the lifetime of the putative iron(III)-superoxo intermediate is too short to allow its interception by TBP-H. The subsequent reaction with residual iron(II) precursor must be strongly favored over the reaction with TBP-H. Clearly, further investigation of the reaction of **3** with $O_2$ and its differences with **1** is warranted.

## A Mechanistic Framework

We have considered the accumulated observations described above and postulate the mechanistic framework illustrated in Scheme 4 to rationalize the different outcomes. We propose an iron(III)-superoxo species as the common intermediate that is formed initially in the oxygenation of **1** and **2**. This species has a number of possible fates (Scheme 4). The bound

superoxide can act as a nucleophile and attack the electrophilic keto carbon of the bidentate α-keto acid to initiate oxidative decarboxylation, according to the generally accepted mechanism for 2-OG-dependent iron enzymes.[6] Alternatively, the bound superoxide can accept an electron from residual iron(II) precursor to form the diiron(III)-peroxo intermediate. Thirdly, the bound superoxide can abstract a hydrogen atom from added phenol. All three outcomes have been observed in the case of **1** depending on the reaction conditions.

These three distinct reactions presumably have different activation barriers. For **1**, oxidative decarboxylation is strongly favored at 25 °C, and the putative iron(IV)-oxo oxidant produced therefrom is able to carry out intramolecular attack of an isopropyl C–H bond on the Tp ligand or intermolecular oxo-atom transfer to THT. In contrast, oxidative decarboxylation does not readily occur at −40 °C; instead a green chromophore identified to be a diiron(III)-peroxo intermediate forms, analogous to that previously reported in the oxygenation of **3**. However peroxo formation can be prevented by the presence of the phenol TBP–H, which is oxidized to TBP•. This interception suggests involvement of a superoxo species that is a precursor of the peroxo intermediate but can also abstract a hydrogen atom from TBP–H.

The reaction energetics are clearly different for **2**. In this case, oxidative decarboxylation is favored both at 25 and −40 °C and the corresponding peroxo intermediate is not observed to form at the lower temperature. This difference in reactivity from **1** suggests that the intramolecular attack of the superoxo moiety on the bound BF in **2** is much more facile at −40 °C than the corresponding attack on the bound PRV in **1**, presumably resulting from the increased electrophilicity of the BF carbonyl carbon because of the more electron withdrawing phenyl group. As a result the superoxo intermediate derived from **2** is too short-lived to allow alternative intermolecular reaction pathways to occur.

Another factor to consider may be the relative basicities of the carboxylate ligands used in this study, as reflected by their aqueous $pK_a$ values. They increase in the order: benzoylformic acid (1.39),[65] pyruvic acid (1.94),[66] benzoic acid (4.19).[67] The differing basicities of the bound carboxylate ligands will modulate the reducing power of the respective iron(II) centers and affect the equilibria that govern the initial $O_2$ binding step and the subsequent reaction of the $O_2$ adduct with a second molecule of [$Fe^{II}(Tp^{iPr2})(O_2CR)$] to form the peroxo intermediate. Thus, formation of the peroxo intermediate should be most favorable for **3**. Indeed, unlike in the oxygenation of **1** at −40 °C, we found that the oxygenation of **3** cannot be prevented by the presence of TBP-H. The fact that the latter reaction occurs only in toluene solvent introduces another mechanistic variable to consider and details of the oxygenation mechanisms of **1** and **3** may differ. Clearly a more in-depth comparison of the oxygenation chemistry of **1** and **3** will be informative.

In conclusion we have described a set of three $Fe^{II}(Tp^{iPr2})$ complexes **1**–**3**, where the ancillary carboxylate or α-keto acid ligand significantly modulates the outcome of the reaction. In all three cases, the initial formation of a common iron(III)-superoxo intermediate is inferred. Under the appropriate conditions, this species derived from **1** can A) act as a nucleophile to initiate the oxidative decarboxylation of the bound α-ketocarboxylate, B) become reduced by another equivalent of iron(II) complex to form a diiron(III)-peroxo intermediate, or C) abstract a hydrogen atom from phenol. On the other hand, **2** reacts with $O_2$ and solely follows pathway A, while **3** follows only pathway B because of the differences in the electronic properties of the ancillary ligand. Iron(III)-superoxo species have also been implicated recently in the reactions of $Fe^{II}$(TMC) and $Fe^{II}$(N4Py) (TMC = 1,4,8,11-tetramethylcyclam; N4Py = *N*,*N*-bis (2-pyridylmethyl)bis(2-pyridyl)methylamine) with $O_2$ in the presence of protons and reductants to form oxoiron(IV) and hydroperoxoiron(III) species, respectively.[63,64] These reactions demonstrate the versatility of the iron(III)-superoxo moiety and support the

mechanistic diversity illustrated in Scheme 2 for the various iron–$O_2$ adducts that must form in the catalytic cycles of nonheme iron oxidases and oxygenases.

## Experimental Section

### General

All reagents and solvents were purchased from commercial sources and were used without further purification unless otherwise noted. Methanol was rigorously dried by distilling from $Mg(OMe)_2$ and degassed under $N_2$ prior to use. Anhydrous dichloromethane and acetonitrile were purchased from Aldrich. Preparation and handling of air-sensitive materials were carried out under an inert atmosphere ($N_2$) in a glovebox. ***Caution!*** *Perchlorate salts are potentally explosive and should be handled with care*.

### Synthesis of 1

To a mixture of ligand (0.126 g, 0.25 mmol) and $Fe(ClO_4)_2$ (0.10 g, 0.25 mmol) in methanol (3 mL), sodium pyruvate (0.029 g 0.25 mmol) was added resulting in an immediate color change of the solution from colorless to red. This cloudy solution was stirred for an hour at room temperature. The solid was then filtered and dried in vacuo. X-ray quality crystals were grown via slow evaporation of a saturated $CH_2Cl_2$ solution at −20°C. Anal. Calcd for 1, $C_{31}H_{53}BFeN_6O_4 \cdot 3CH_2Cl_2$ (895.3 g/mol): C, 45.61; H, 6.64; N, 9.39. Found: C, 45.54; H, 6.70; N, 9.30. UV- vis [$\lambda_{max}$, nm (ε, $M^{-1}cm^{-1}$) in MeCN]: 458 (sh, 460), 500 (510), 540 (sh, 390). $^1$H-NMR (benzene-d6, 300 MHz, 25 °C): −7.8 (s, B*H*), −2.8 (s, C*H*$Me_2$) 3.7 (s, CH*Me*$_2$), 14.4 (s, C*H*$Me_2$), 8.04 (s, C*H*$Me_2$), 63.7 (s, pz-4-*H*), 114.8 (s, $O_2$CC(O)C*H*$_3$).

### Synthesis of 2

To a mixture of ligand (0.126 g, 0.25 mmol) and $Fe(OTf)_2 \cdot 2MeCN$[65] (0.10 g, 0.25 mmol) in methylene chloride (3 mL), solid sodium benzoylformate (0.043 g 0.25 mmol) was added. The solution turned blue immediately and was stirred for an hour at room temperature. The solid was filtered and dried in vacuo. X-ray quality crystals were grown via slow evaporation of a saturated pentane solution at −20° C. Anal. Calcd for 2, $C_{35}H_{51}BFeN_6O_3$ (670.47 g/mol): C, 62.70; H, 7.67; N, 12.53. Found: C, 62.92; H, 7.83; N, 12.47. UV- vis [$\lambda_{max}$, nm (ε, $M^{-1}cm^{-1}$) in MeCN]: 553 (sh, 510), 610 (610). $^1$H-NMR (benzene-$d_6$, 300 MHz, 25 °C): −8.1 (s, B*H*), −1.78 (s, C*H*$Me_2$) 3.8 (s, CH*Me*$_2$), 13.2 (s, C*H*$Me_2$), 20.3 (*o*-BF), 16.7 (*m*-BF), 63.8 (s, pz-4-*H*).

### Identification of ligand hydroxylation product by NMR spectroscopy

5 mM **1** in 2 mL MeCN was bubbled with $O_2$ using a balloon and the solution was stirred vigorously for 15 minutes. To this solution was added *ca.* 2 mL of 1 M HCl with vigorous stirring. To the above solution excess $NH_3$ (aq) was added and organic products were extracted with diethyl ether. The extract was dried over $MgSO_4$ and to this solution 1,4-dimethoxybenzene was added as an internal standard. Evaporation of solvent resulted in colorless residue soluble in $CDCl_3$ that was analyzed by $^1$H-NMR spectroscopy.

### Identification of the acid decarboxylation product by NMR spectroscopy

5 mM **2** in 2 mL MeCN was bubbled with $O_2$ using a balloon and the solution was stirred vigorously for 15 minutes. To this solution was added *ca* 2 mL 3 M HCl with vigorous stirring. The organic layer was extracted with diethyl ether and washed with distilled water. The extract was then dried over $MgSO_4$ and to this solution 1,4-dimethoxybenzene was added as an internal standard. Evaporation of solvent resulted in a faintly colored residue soluble in $CDCl_3$ that was analyzed by $^1$H-NMR spectroscopy.

### Crystallography of 1 and 2

For both complexes a crystal (approximate dimensions 0.40 × 0.35 × 0.30 $mm^3$) was placed onto the tip of a 0.1 mm diameter glass capillary and mounted on a CCD area detector diffractometer for data collection at 173(2) K.[66] A preliminary set of cell constants was calculated from reflections harvested from three sets of 20 frames for **1** and four sets of 30 frames for **2**. These initial sets of frames were oriented such that orthogonal wedges of reciprocal space were surveyed. This produced initial orientation matrices determined from 101 reflections for **1** and 324 reflections for **2**. The data collection was carried out using MoKα radiation (graphite monochromator) with a frame time of 20 seconds for **1** and 45 seconds for **2** and a detector distance of 4.9 cm. A randomly oriented region of reciprocal space was surveyed to the extent of one sphere and to a resolution of 0.82 Å for **1** (0.80 Å for **2**). Four major sections of frames were collected with 0.30° steps in ω at four different φ settings and a detector position of −28° in 2θ. The intensity data were corrected for absorption and decay (SADABS).[67] Final cell constants were calculated from 2801 (for **1**) and 2982 (for **2**) strong reflections from the actual data collection after integration (SAINT).[68] Please refer to Table S1 for additional crystal and refinement information.

The structures were solved and refined using SHELXTL.[69] The space groups of P-1 (for **1**) and P2/c (for **2**) were determined based on systematic absences and intensity statistics. A direct-methods solution was calculated, which provided most non-hydrogen atoms from the E-map. Full-matrix least squares/difference Fourier cycles were performed which located the remaining non-hydrogen atoms. All non-hydrogen atoms were refined with anisotropic displacement parameters. All hydrogen atoms were placed in ideal positions and refined as riding atoms with relative isotropic displacement parameters. The final full matrix least squares refinement converged to $R1 = 0.0473$ for **1** and 0.0416 for **2** and $wR2 = 0.1358$ for **1** and 0.1100 for **2** ($F^2$, all data).

### Physical Methods

Elemental analyses were performed by Atlantic Microlab, Inc. UV/vis spectra were recorded on a HP 8452A diode-array spectrometer with samples maintained at low temperature using a cryostat from Unisoku Scientific Instruments, Osaka, Japan. ESI-MS studies were performed by using Bruker BioTOF mass spectrometer and the data processing was done by using Bruker Daltonics software. NMR spectra were recorded on a Varian VXR-300 spectrometer at room temperature. Resonance Raman spectra were collected using an excitation wavelength of 647.1 nm from a Spectra-Physics Model 2060 krypton ion laser and an ACTON AM-506 monochromator equipped with a Princeton LN/CCD data collection system. Low temperature spectra in $CH_3CN$ were obtained at 77 K using a 135° backscattering geometry. Samples were frozen onto a gold-plated copper cold finger in thermal contact with a Dewar flask containing liquid nitrogen. Raman frequencies were calibrated to indene prior to data collection. The monochromator slit width was set for a band-pass of 4 $cm^{-1}$ for all spectra. rR spectra were intensity corrected to the 773 $cm^{-1}$ solvent peak. Mössbauer spectra were recorded with two spectrometers, using Janis Research Super-Varitemp dewars that allowed studies in applied magnetic fields up to 8.0 T in the temperature range from 1.5 to 200 K. Mössbauer spectral simulations were performed using the WMOSS software package (WEB Research, Edina, MN). Isomer shifts are quoted relative to Fe metal at 298 K.

## Supplementary Material

Refer to Web version on PubMed Central for supplementary material.

## Acknowledgments

This work was supported by the National Institutes of Health (grants GM-33162 to L.Q. and EB-001475 to E.M. and postdoctoral fellowship ES017390-01 to M.A.C.) and by the Kurata Foundation (to K.F.). A.M. is grateful for a dissertation fellowship from the University of Minnesota Graduate School. We thank Dr. Victor G. Young, Jr. and the X-Ray Crystallographic Laboratory of University of Minnesota for crystallographic assistance.

## References

1. Solomon EI, Brunold TC, Davis MI, Kemsley JN, Lee SK, Lehnert N, Neese F, Skulan AJ, Yang YS, Zhou J. Chem Rev 2000;100:235–349. [PubMed: 11749238]
2. Costas M, Mehn MP, Jensen MP, Que L Jr. Chem Rev 2004;104:939–986. [PubMed: 14871146]
3. Hausinger RP. Crit Rev Biochem Mol Biol 2004;39:21–68. [PubMed: 15121720]
4. Kovaleva EG, Lipscomb JD. Nature Chem Biol 2008;4:186–193. [PubMed: 18277980]
5. Loenarz C, Schofield CJ. Nature Chem Biol 2008;4:152–156. [PubMed: 18277970]
6. Hanauske-Abel HM, Günzler V. J Theor Biol 1982;94:421–455. [PubMed: 6281585]
7. Hanauske-Abel HM, Popowicz AM. Current Medicinal Chemistry 2003;10:1005–1019. [PubMed: 12678673]
8. Krebs C, Galonić Fujimori D, Walsh CT, Bollinger JM Jr. Acc Chem Res 2007;40:484–492. [PubMed: 17542550]
9. Price JC, Barr EW, Hoffart LM, Krebs C, Bollinger JM Jr. Biochemistry 2005;44(22):8138–8147. [PubMed: 15924433]
10. Galonic DP, Barr EW, Walsh CT, Bollinger JM Jr, Krebs C. Nature Chem Biol 2007;3:113–116. [PubMed: 17220900]
11. Bollinger JM Jr, Krebs C. Curr Opin Chem Biol 2007;11:151–158. [PubMed: 17374503]
12. Wolfe MD, Parales JV, Gibson DT, Lipscomb JD. J Biol Chem 2001;276:1945–1953. [PubMed: 11056161]
13. Wolfe MD, Altier DJ, Stubna A, Popescu CV, Münck E, Lipscomb JD. Biochemistry 2002;41:9611–9626. [PubMed: 12135383]
14. Wolfe MD, Lipscomb JD. J Biol Chem 2003;278:829–835. [PubMed: 12403773]
15. Kovaleva EG, Lipscomb JD. Science 2007;316:453–457. [PubMed: 17446402]
16. Cicchillo RM, Zhang H, Blodgett JAV, Whitteck JT, Li G, Nair SK, van der Donk WA, Metcalf WW. Nature 2009;459:871–874. [PubMed: 19516340]
17. Evans JP, Ahn K, Klinman JP. J Biol Chem 2003;278:49691–49698. [PubMed: 12966104]
18. Chen P, Solomon EI. J Am Chem Soc 2004;126:4991–5000. [PubMed: 15080705]
19. Gunderson WA, Zatsman AI, Emerson JP, Farquhar ER, Que L Jr, Lipscomb JD, Hendrich MP. J Am Chem Soc 2008;130:14465–14467. [PubMed: 18839948]
20. Emerson JP, Kovaleva EG, Farquhar ER, Lipscomb JD, Que L Jr. Proc Natl Acad Sci USA 2008;105:7347–7352. [PubMed: 18492808]
21. Bollinger JM Jr, Diao Y, Matthews ML, Xing G, Krebs C. Dalton Trans 2009:905–914. [PubMed: 19173070]
22. Brown PM, Caradoc-Davies TT, Dickson JMJ, Cooper GJS, Loomes KM, Baker EN. Proc Natl Acad Sci USA 2006;103:15032–15037. [PubMed: 17012379]
23. Xing G, Barr EW, Diao Y, Hoffart LM, Prabhu KS, Arner RJ, Reddy CC, Krebs C, Bollinger JM Jr. Biochemistry 2006;45:5402–5412. [PubMed: 16634621]
24. Xing G, Diao Y, Hoffart LM, Barr EW, Prabhu KS, Arner RJ, Reddy CC, Krebs C, Bollinger JM Jr. Proc Natl Acad Sci USA 2006;103:6130–6135. [PubMed: 16606846]
25. Karlsson A, Parales JV, Parales RE, Gibson DT, Eklund H, Ramaswamy S. Science 2003;299:1039–1042. [PubMed: 12586937]
26. Zhang Y, Colabroy KL, Begley TP, Ealick SE. Biochemistry 2005;44:7632–7643. [PubMed: 15909978]
27. Momenteau M, Reed CA. Chem Rev 1994;94:659–698.

28. Roelfes G, Vrajmasu V, Chen K, Ho RYN, Rohde JU, Zondervan C, la Crois RM, Schudde EP, Lutz M, Spek AL, Hage R, Feringa BL, Münck E, Que L Jr. Inorg Chem 2003;42:2639–2653. [PubMed: 12691572]
29. Koehntop KD, Rohde JU, Costas M, Que L Jr. Dalton Trans 2004:3191–3198. [PubMed: 15483700]
30. Que L Jr. J Biol Inorg Chem 2004;9:684–690. [PubMed: 15300470]
31. Lipscomb, JD.; Orville, AM. Metal Ions in Biological Systems. Sigel, H.; Sigel, A., editors. Vol. 28. Marcel Dekker; New York: 1992. p. 243-298.
32. Ookubo T, Sugimoto H, Nagayama T, Masuda H, Sato T, Tanaka K, Maeda Y, Okawa H, Hayashi Y, Uehara A, Suzuki M. J Am Chem Soc 1996;118:701–702.
33. Dong Y, Yan S, Young VG Jr, Que L Jr. Angew Chem Int Ed Engl 1996;35:618–620.
34. Kim K, Lippard SJ. J Am Chem Soc 1996;118:4914–4915.
35. Shan X, Que L Jr. Proc Natl Acad Sci USA 2005;102:5340–5345. [PubMed: 15802473]
36. Cramer CJ, Tolman WB. Acc Chem Res 2007;40:601–608. [PubMed: 17458929]
37. Würtele C, Gaoutchenova E, Harms K, Holthausen MC, Sundermeyer J, Schindler S. Angew Chem Int Ed 2006;45:3867–3869.
38. Maiti D, Fry HC, Woertink JS, Vance MA, Solomon EI, Karlin KD. J Am Chem Soc 2007;129:264–265. [PubMed: 17212392]
39. Maiti D, Lee DH, Gaoutchenova K, Würtele C, Holthausen MC, Sarjeant AAN, Sundermeyer J, Schindler S, Karlin KD. Angew Chem Int Ed 2008;47:82–85.
40. Kunishita A, Kubo M, Sugimoto H, Ogura T, Sato K, Takui T, Itoh S. J Am Chem Soc 2009;131:2788–2789.
41. Zhao M, Helms B, Slonkina E, Friedle S, Lee D, DuBois J, Hedman B, Hodgson KO, Fréchet JMJ, Lippard SJ. J Am Chem Soc 2008;130:4352–4363. [PubMed: 18331028]
42. Kitajima N, Fukui H, Moro-oka Y, Mizutani Y, Kitagawa T. J Am Chem Soc 1990;112:6402–6403.
43. Kitajima N, Tamura N, Amagai H, Fukui H, Moro-oka Y, Mizutani Y, Kitagawa T, Mathur R, Heerwegh K, Reed CA, Randall CR, Que L Jr, Tatsumi K. J Am Chem Soc 1994;116:9071–9085.
44. Karlin KD, Wei N, Jung B, Kaderli S, Niklaus P, Zuberbühler AD. J Am Chem Soc 1993;115:9506–9514.
45. Ha EH, Ho RYN, Kesiel JF, Valentine JS. Inorg Chem 1995;34:2265–2266.
46. Hegg EL, Ho RYN, Que L Jr. J Am Chem Soc 1999;121:1972–1973.
47. Mehn MP, Fujisawa K, Hegg EL, Que L Jr. J Am Chem Soc 2003;125:7828–7842. [PubMed: 12823001]
48. Fujisawa K, Tada N, Nishida Y, Miyashita Y, Okamoto K-i. Inorg Chem Comm 2008;11:381–384.
49. Mukherjee A, Martinho M, Bominaar EL, Münck E, Que L Jr. Angew Chem Int Ed 2009;48:1780–1783.
50. Chiou YM, Que L Jr. J Am Chem Soc 1995;117:3999–4013.
51. Paine TK, Zheng H, Que L Jr. Inorg Chem 2005;44:474–476. [PubMed: 15679371]
52. Hikichi S, Ogihara T, Fujisawa K, Kitajima N, Akita M, Moro-Oka Y. Inorg Chem 1997;36:4539–4547. [PubMed: 11670119]
53. Kitajima N, Osawa M, Tanaka M, Moro-oka Y. J Am Chem Soc 1991;113:8952–8953.
54. Reinaud OM, Theopold KH. J Am Chem Soc 1994;116:6979–6980.
55. Goldsmith CR, Jonas RT, Stack TDP. J Am Chem Soc 2002;124:83–96. [PubMed: 11772065]
56. Roelfes G, Lubben M, Chen K, Ho RYN, Meetsma A, Genseberger S, Hermant RM, Hage R, Mandal SK, Young VG Jr, Zang Y, Kooijman H, Spek AL, Que L Jr, Feringa BL. Inorg Chem 1999;38:1929–1936. [PubMed: 11670967]
57. Girerd JJ, Banse F, Simaan AJ. Struct Bonding 2000;97:145–177.
58. Fiedler AT, Shan X, Mehn MP, Kaizer J, Torelli S, Frisch JR, Kodera M, Que L Jr. J Phys Chem A 2008;112:13037–13044. [PubMed: 18811130]
59. Kauffmann, K.; Münck, E. Spectroscopic Methods in Bioinorganic Chemistry. Solomon, EI.; Hodgson, KO., editors. American Chemical Society; Washington, D. C: 1998. p. 16-29.
60. Krebs C, Bollinger JM Jr, Theil EC, Huynh BH. J Biol Inorg Chem 2002;7:863–869. [PubMed: 12203023]

61. Frisch JR, Vu VV, Martinho M, Münck E, Que L Jr. Inorg Chem 2009;48:8325–8336. [PubMed: 19610611]
62. Zhang X, Furutachi H, Fujinami S, Nagatomo S, Maeda Y, Watanabe Y, Kitagawa T, Suzuki M. J Am Chem Soc 2005;127:826–827. [PubMed: 15656607]
63. LeCloux DD, Barrios AM, Mizoguchi TJ, Lippard SJ. J Am Chem Soc 1998;120:9001–9014.
64. LeCloux DD, Barrios AM, Lippard SJ. Bioorg Med Chem 1999;7:763–772. [PubMed: 10400329]
65. Wheatley MS. Experientia 1956;12:339–340.
66. Chiang Y, Kresge AJ, Pruszynski P. J Am Chem Soc 1992;114:3103–3107.
67. Lide, DR. CRC Handbook of Chemistry and Physics. 73. CRC Press; Boca Raton, FL: 1992. p. 8-39.

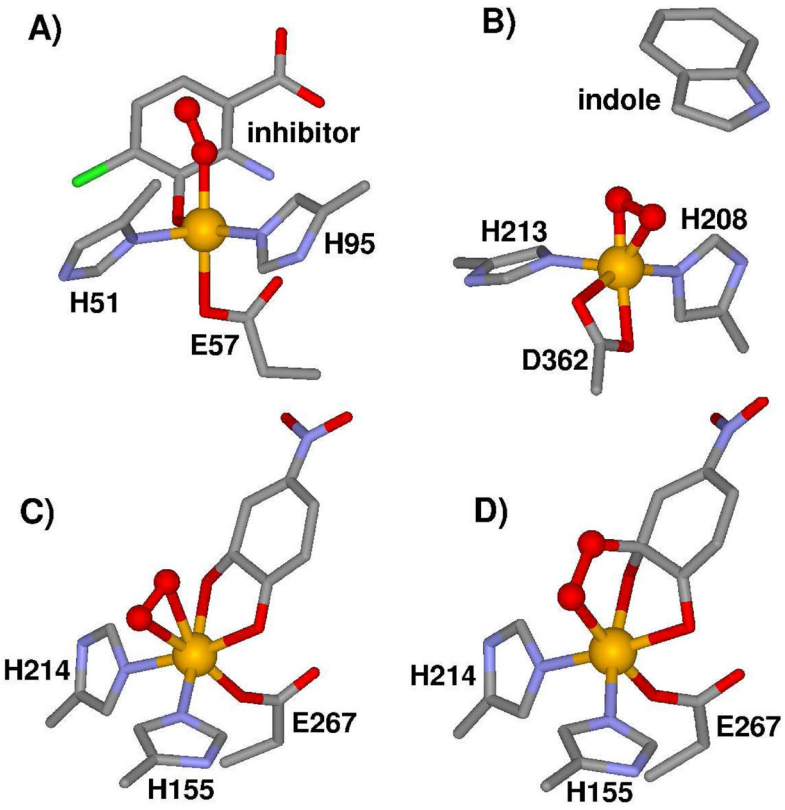


**Figure 1.**

Active site structures of the $O_2$ adducts of nonheme iron enzymes that have been structurally characterized by X-ray crystallography (orange Fe, grey C, red O, blue N, green Cl). A) The end-on $O_2$ adduct of 3-hydroxyanthranilate-3,4-dioxygenase from *R. metallidurans* complexed with an inhibitor (1YFW.pdb). B) The side-on $O_2$ adduct NDO from *Pseudomonas* sp. in the presence of the substrate analog indole (1O7N.pdb). C) and D) The side-on $O_2$ adduct of the HPCD-4-nitrocatechol complex of *B. fuscum* found in subunit C and the subsequent alkylperoxo intermediate found in subunits B and D, respectively (2IGA.pdb).

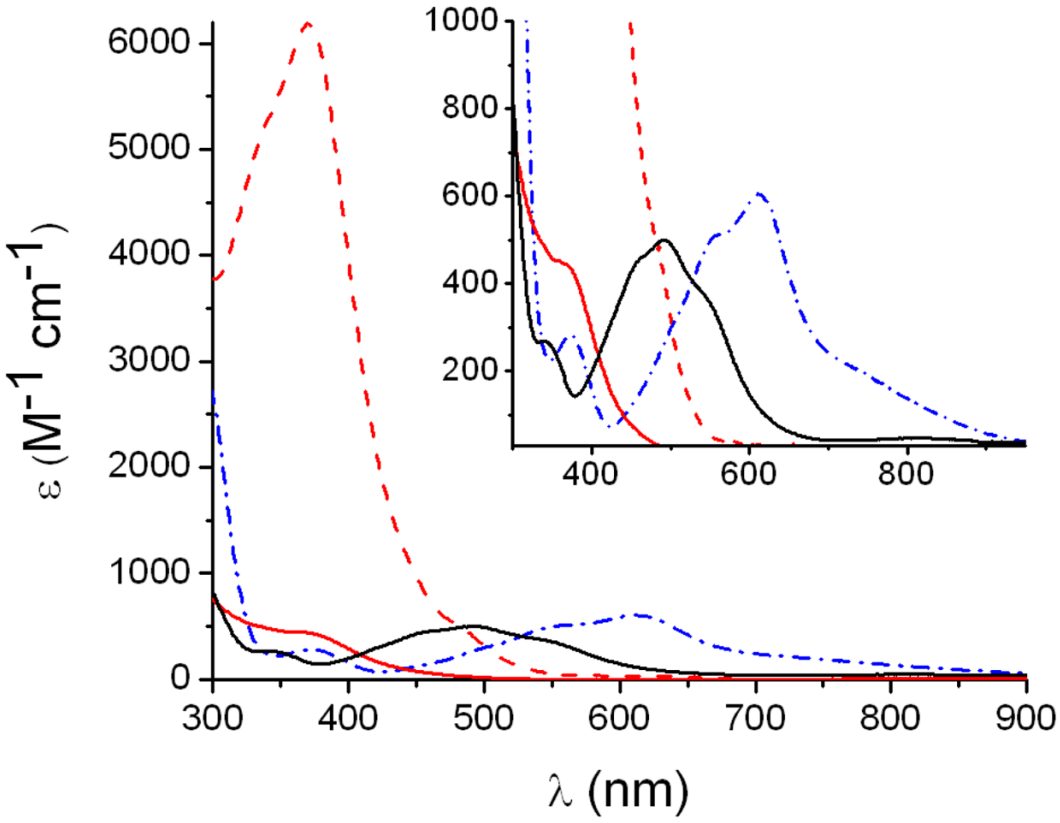


**Figure 2.**
UV-Vis spectra in MeCN of **1** (black solid line), **2** (blue dashed-dotted line), the yellow solution obtained upon oxygenation (red dashed line) and the solution obtained upon oxygenation in the presence of THT (red solid line). Inset shows the corresponding magnified spectra in the visible region.

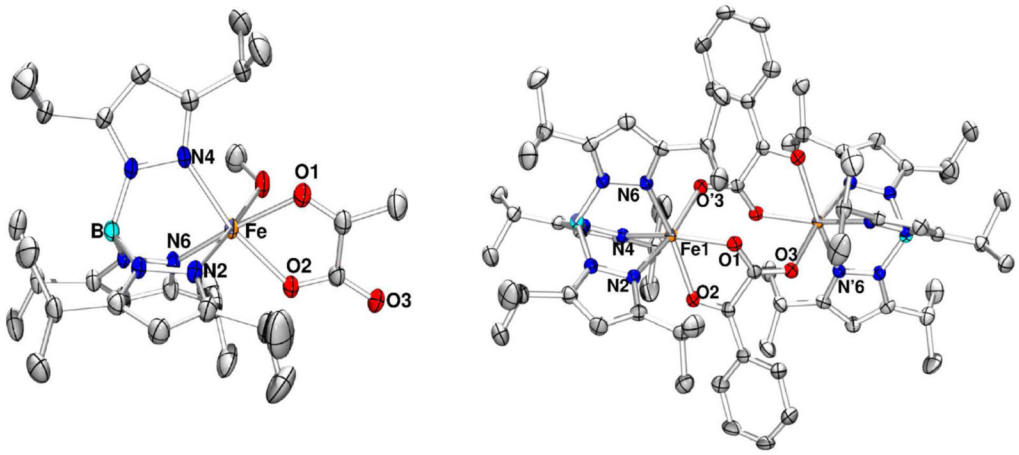


**Figure 3.**
ORTEP plots for [Fe(Tp$^{iPr2}$)(PRV)(MeOH)] (**1**) and [Fe(Tp$^{iPr2}$)(BF)] (**2**). Hydrogen atoms are omitted for clarity.

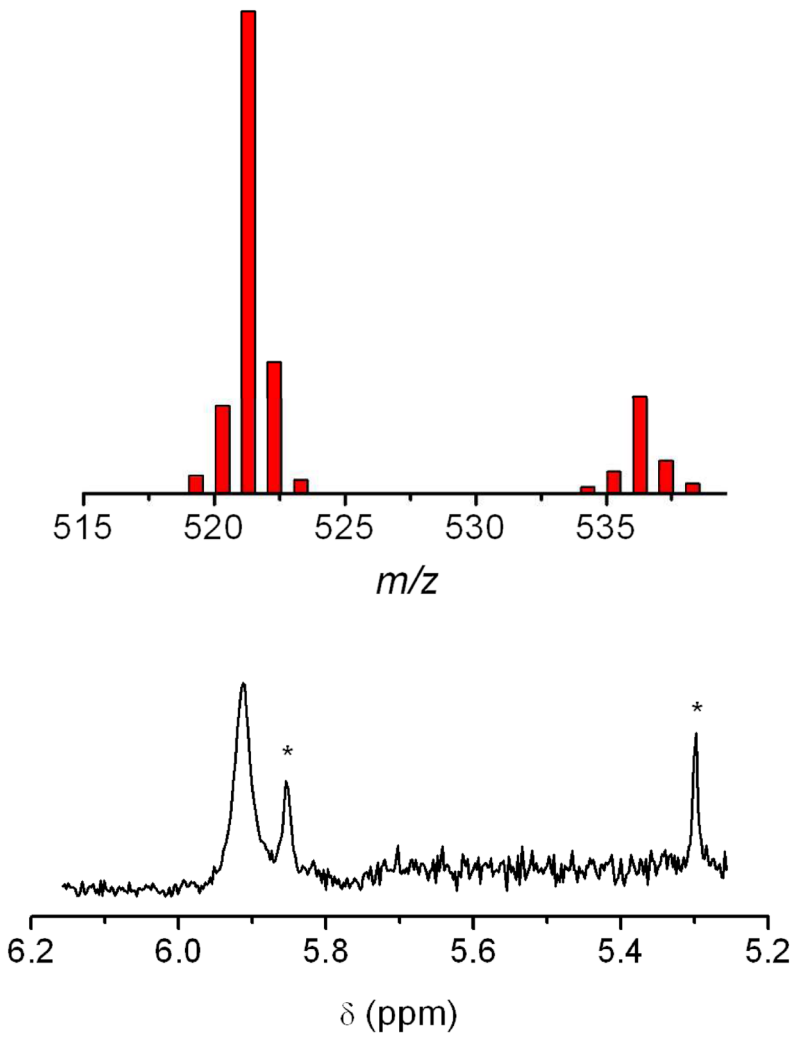


**Figure 4.**

Top: ESI-MS spectrum of **1** after oxygenation but prior to acid treatment. Bottom: $^{1}$H-NMR spectrum in the 5.2–6.2-ppm region of the pyrazoles in $CDCl_3$ obtained from the reaction of **1** with $O_2$ after acid treatment to decompose the $Tp^{iPr2*}$ ligand (|-marked peaks arise from 3-isopropenyl-5-isopropylpyrazole; the peak at 5.90 ppm is the 4-*H* of the 3,5-diisopropylpyrazole).

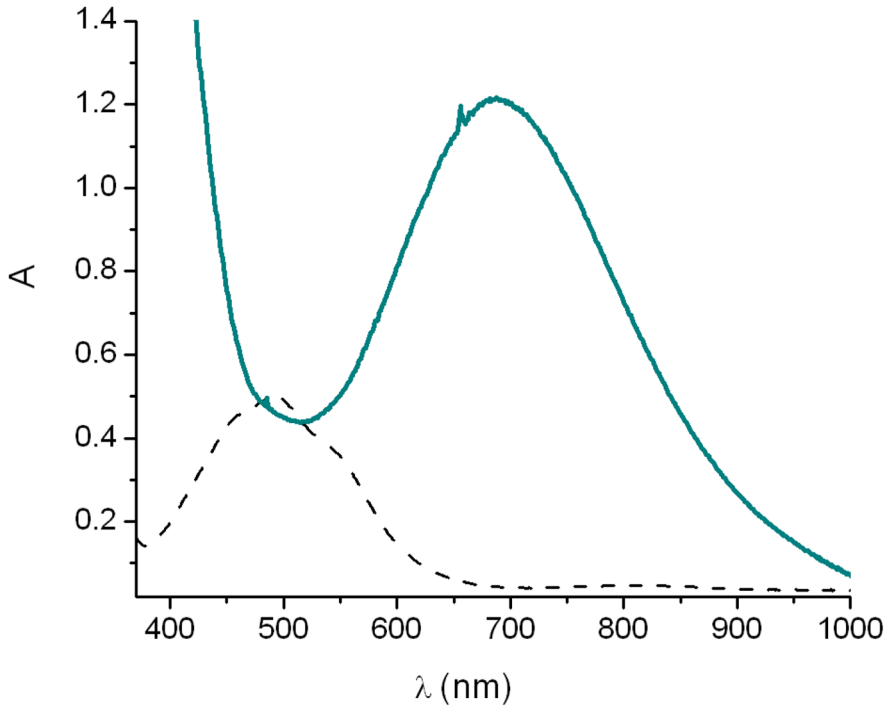


**Figure 5.**

Oxygenation of 1 mM [$Fe^{II}(Tp^{iPr2})$(PRV)] (**1**) (dashed line) at −40°C in MeCN resulting in the formation of a green chromophore (solid line) that is assigned to a (μ-1,2-peroxo)diiron (III) complex.

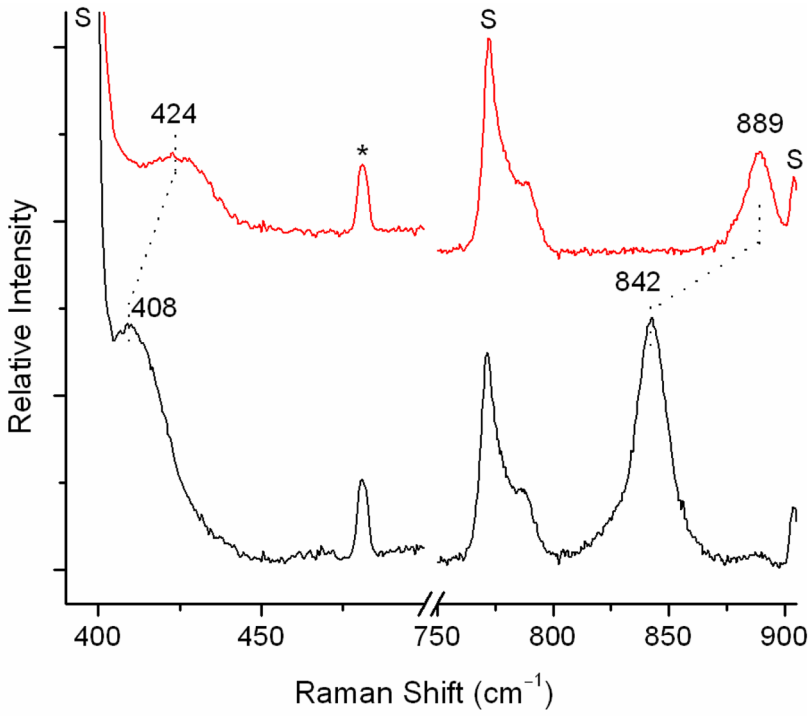


**Figure 6.**

Resonance Raman spectra using $\lambda_{ex}$ = 647.1 nm of the green chromophore from the oxygenation of **1** at −40 °C in MeCN with $^{16}O_2$ (top) and $^{18}O_2$ (bottom). Solvent peaks are denoted as “S” and the asterisk denotes a laser plasma line.

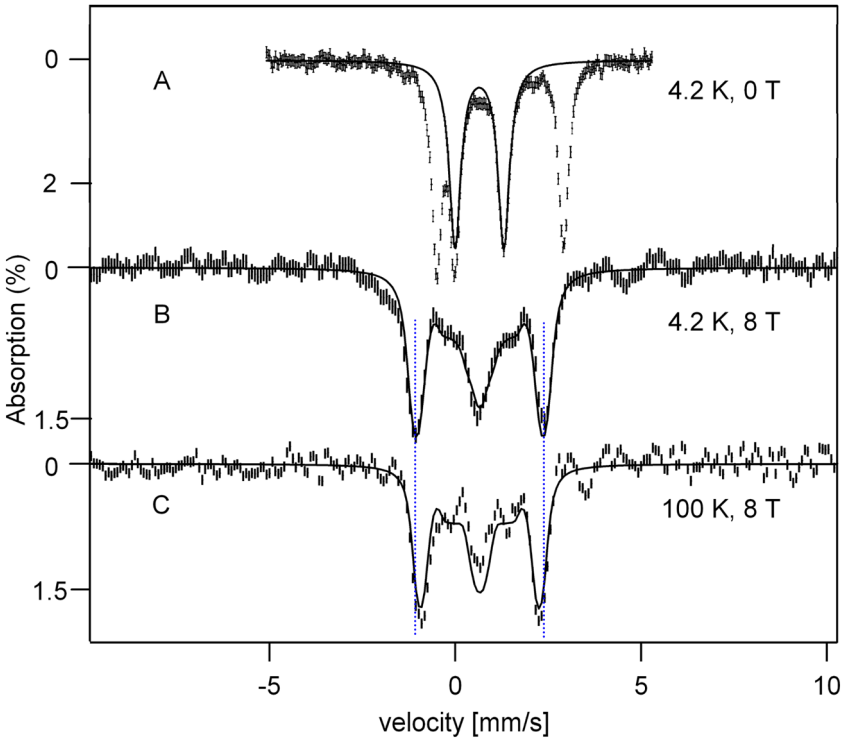


**Figure 7.**

Mössbauer spectra of the green solution obtained from the oxygenation of **1** in MeCN at −40 °C. (A) Spectrum recorded for B = 0. The solid line outlines the contribution of the peroxo intermediate (45% of Fe). (B) and (C) Spectra of the peroxo intermediate recorded in a parallel field of B = 8.0 T at the temperatures indicated; features arising from the $Fe^{II}$ and mononuclear $Fe^{III}$ species were removed as described in Supporting Information. Solid lines in (B) and (C) are spectral simulations for $J = 70\ cm^{-1}$. Hyperfine parameters are: $A_0/g_n\beta_n = -21$ T, $\Delta E_Q = +1.32$ mm/s, $\eta = 1$, and $\delta = 0.65$ mm/s for both sites; the Hamiltonian is given in SI.

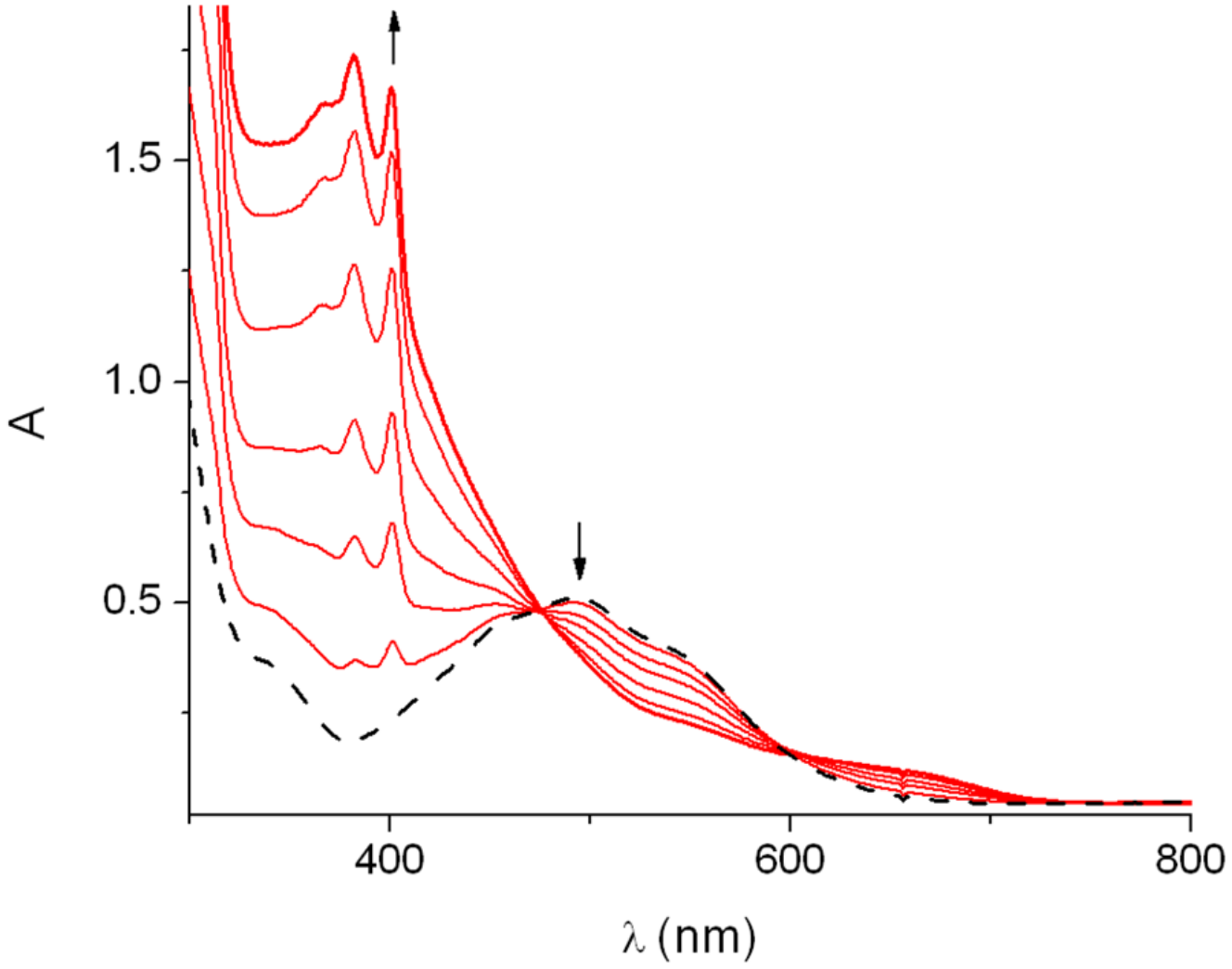


**Figure 8.**
Oxygenation of 1 mM [Fe(Tp$^{iPr2}$)PRV](black line) at −40°C in MeCN in the presence of 1 equiv TBP-H in a 1-cm cuvette. Red lines show the growth of TBP• features.

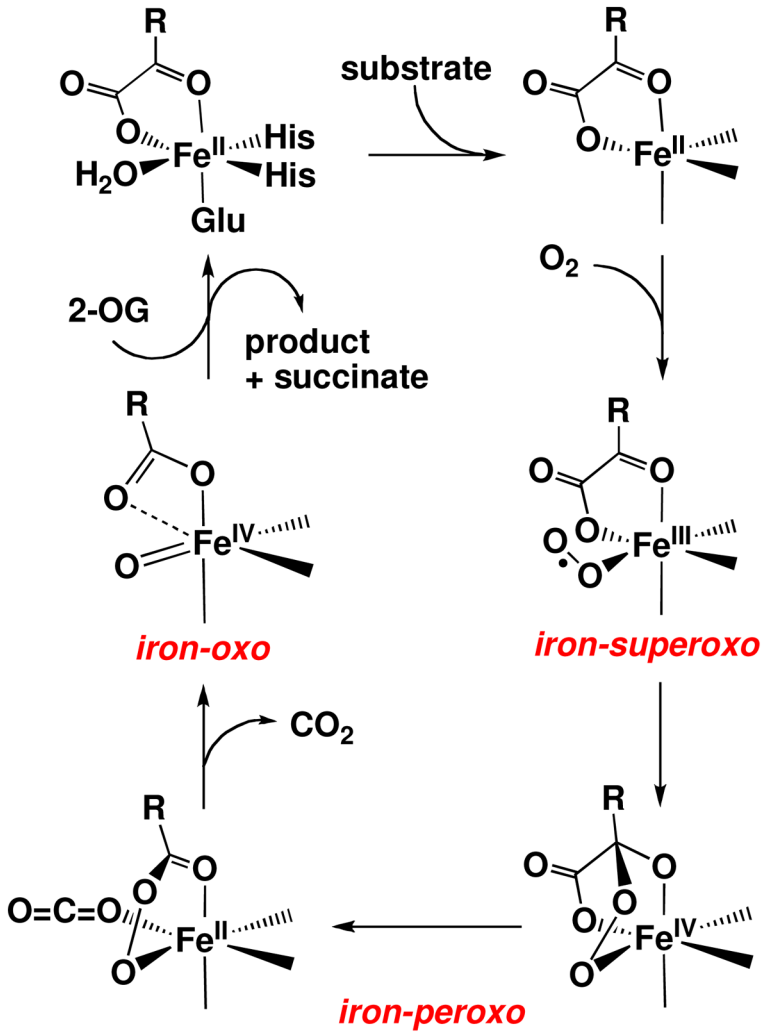


**Scheme 1.**
General mechanism for 2-OG-dependent iron enzymes

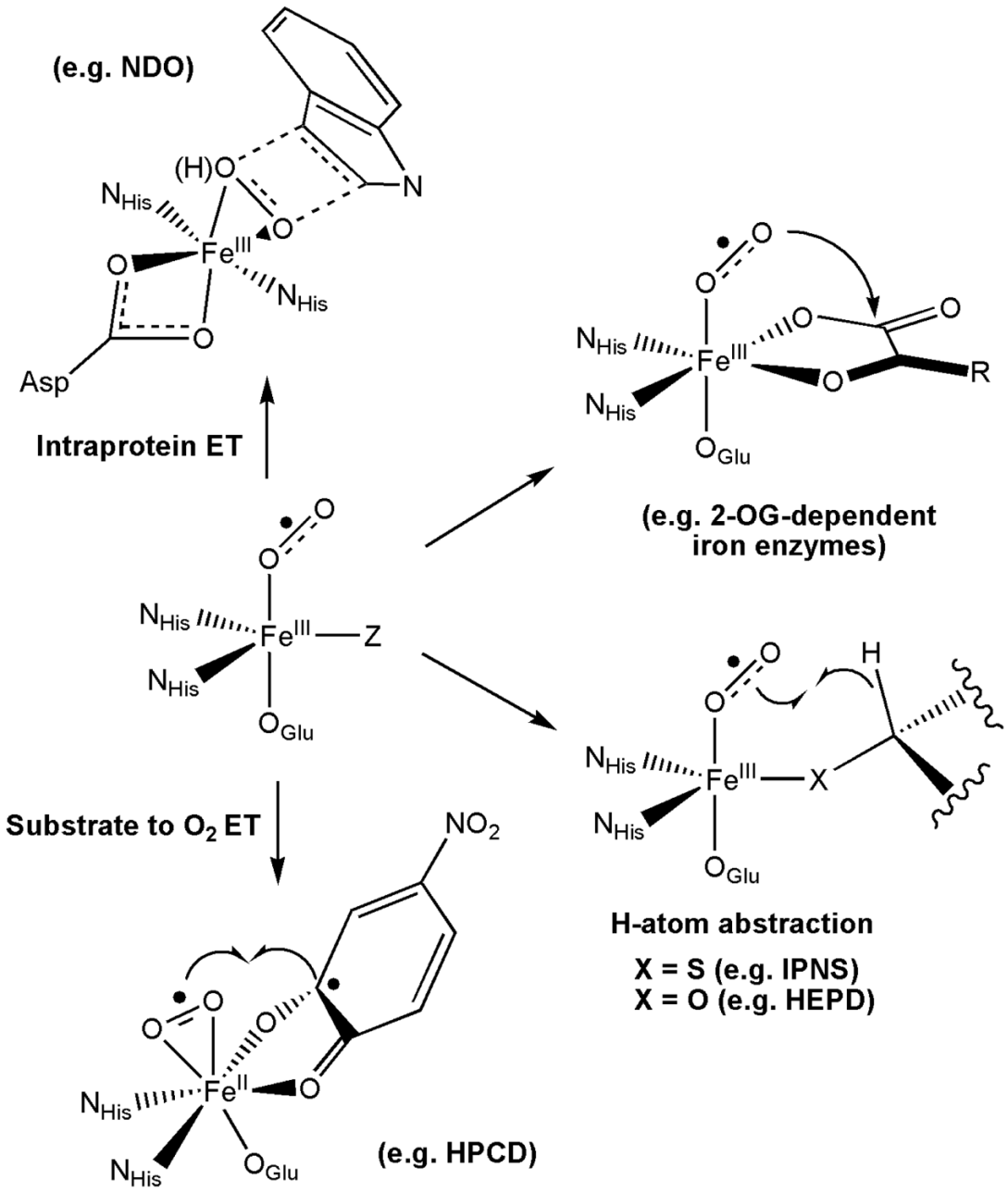


**Scheme 2.**
Various proposed roles for the initial iron-dioxygen adducts in reaction pathways of 2-His-1-carboxylate iron enzymes.

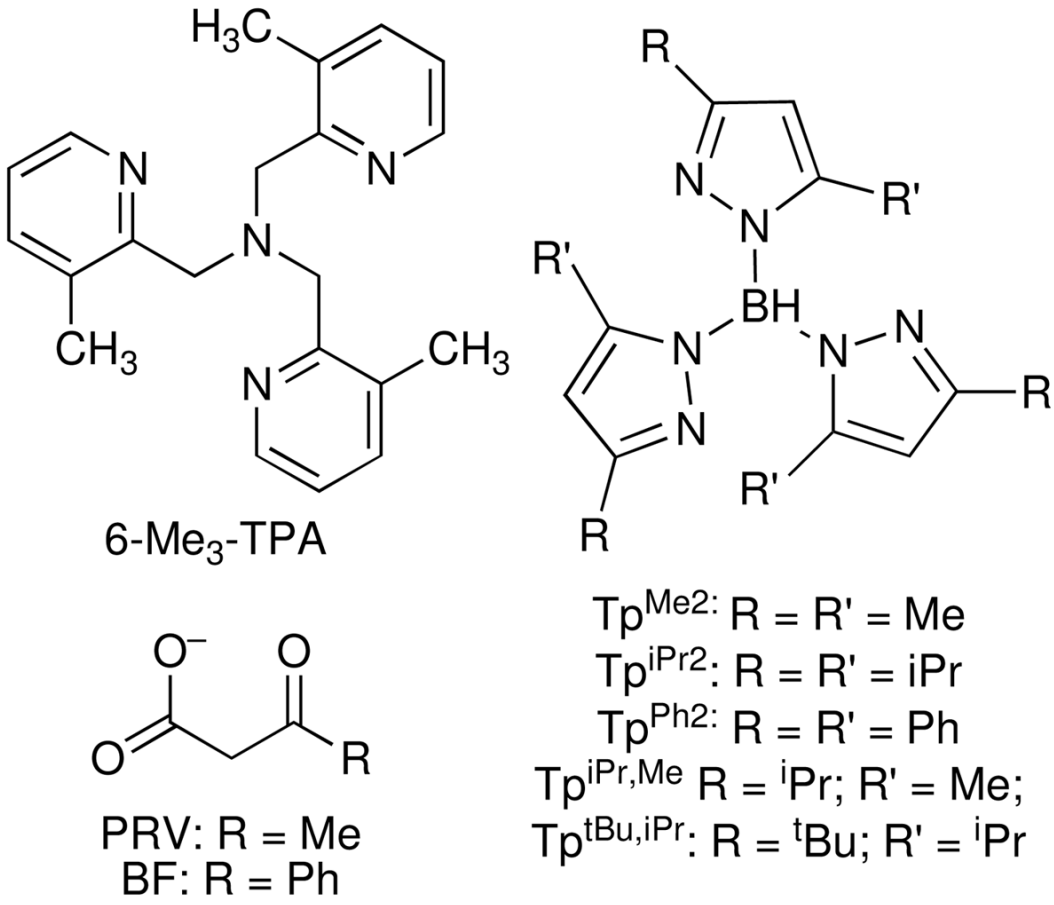


**Scheme 3.**
Ligands.

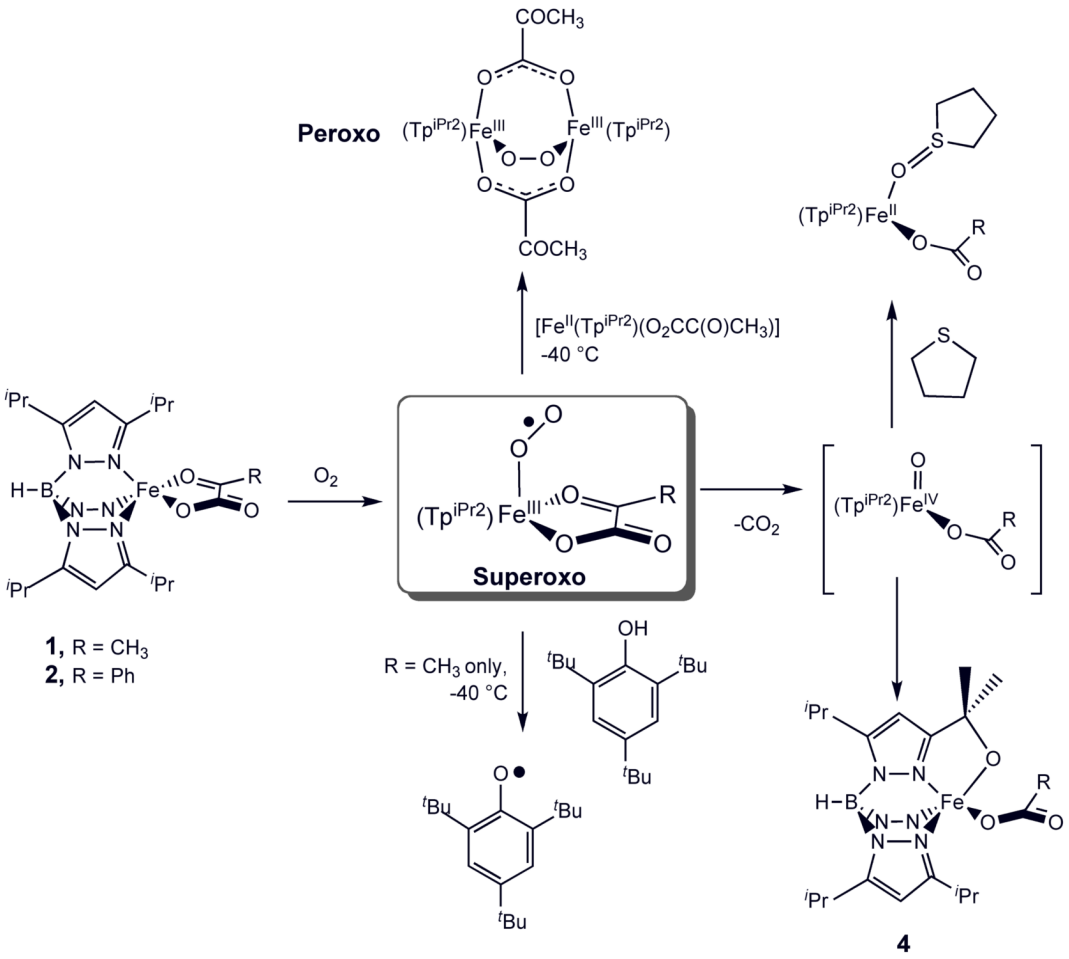


**Scheme 4.**
Reactions of [$Fe^{II}(Tp^{iPr2})X$] complexes with dioxygen.

**Table 1**

Comparison of selected bond lengths of **1** and **2** with those of related structures.

| | **1** | **2** | **[Fe(Tp$^{Ph2}$)(PRV)]**$^a$ | **[Fe(Tp$^{Ph2}$)(BF)]**$^a$ | **[Fe(Tp$^{tBu,iPr}$)(BF)]**$^b$ |
|---|---|---|---|---|---|
| | | 2.1691(15) | | | |
| Fe–$O_{carboxylato}$ | 2.1180(18) | 2.1832(15)$^c$ | 1.967(5) | 1.968(4) | 1.975(7) |
| Fe–$O_{keto}$ | 2.2294(18) | 2.2514(15) | 2.242(6) | 2.206(5) | 2.261(7) |
| Fe–N2 | 2.181(2) | 2.1954(17) | 2.163(6) | 2.188(5) | 2.116(9) |
| Fe–N4 | 2.138(2) | 2.1041(17) | 2.088(8) | 2.068(5) | 2.173(9) |
| Fe–N6 | 2.139(2) | 2.0919(17) | 2.106(8) | 2.086(5) | 2.112(9) |
| C2–$C3_{\alpha\text{-ketoacid}}$ | 1.483(4) | 1.475(3) | 1.498(9) | | |

$^a$ref # 47.

$^b$ref # 52.

$^c$corresponding to r(Fe1–O3′)

## Table 2

Comparison of spectroscopic properties of the peroxo intermediate derived from **1** with similar complexes ($^{18}O$ isotope shifts indicated in parentheses).

| | $\delta(\Delta E_Q)$ mm/s (mm/s) | $\lambda_{max}$ ($\varepsilon$) nm ($M^{-1}$ $cm^{-1}$) | ν(O–O) $cm^{-1}$ | ν(Fe–O) $cm^{-1}$ |
|---|---|---|---|---|
| Peroxo intermediate (obtained from **1**+ $O_2$) | 0.65 (1.32) | 680 (2500) | 889 (−47) | 424 (−16) |
| $[Fe^{III}_2(\mu\text{-}1,2\text{-}O_2)(\mu\text{-}O_2CPh)_2(Tp^{iPr2})_2]$ [a] | -- | 682 (3450) | 876 (−48) | 421 (−12) |
| $[Fe^{III}_2(\mu\text{-}1,2\text{-}O_2)(\mu\text{-}O_2CCH_2Ph)_2(Tp^{iPr2})_2]$ [b] | 0.66 (1.40) | 694 (2650) | 888 (−46) | 415 (−11) |
| $[Fe^{III}_2(\mu\text{-}O)(\mu\text{-}1,2\text{-}O_2)(6\text{-}Me_2BPP)]^{2+}$ [c] | 0.50 (1.31) | 644 (3000) | 847 (−33) | 465 (−19) |
| $[Fe^{III}_2(\mu\text{-}1,2\text{-}O_2)(N\text{-Et-HPTB})(OPPh_3)_2]^{2+}$ [d] | 0.51 (0.80) | 588 (1500) | 900 (−50) | 471 (−16) |
| $[Fe^{III}_2(\mu\text{-}O)(\mu\text{-}1,2\text{-}O_2)(6\text{-Me-BQPA})]^{2+}$ [d] | -- | not reported | 853 (−45) | 463 (−15) |
| $[Fe^{III}_2(\mu\text{-}O)(\mu\text{-}1,2\text{-}O_2)(BQPA)]^{2+}$ [d] | -- | 620 (1000) | 844 (−44) | 464 (−17) |

[a] Ref #43.

[b] Ref #34.

[c] Ref #62; 6-$Me_2$BPP = *N*,*N*-bis(6-methyl-2-pyridylmethyl)-3-aminopropionate.

[d] Ref #58; *N*-Et-HPTB = anion of *N*,*N*,*N*′,*N*′–tetrakis(2-benzimidazolylmethyl)-2-hydroxy-1,3-diaminopropane; BQPA = bis(2-quinolylmethyl)-2-pyridylmethylamine.